ENTRAINMENT IN THE SEPARATED AND REATTACHING FLOW INDUCED BY A WALL-MOUNTED FENCE

Sicheng Li
Fluid Mechanics Key Laboratory of Education Ministry
Beihang University
Beijing 100191, China
lisicheng@buaa.edu.cn

Jinjun Wang
Fluid Mechanics Key Laboratory of Education Ministry
Beihang University
Beijing 100191, China
jjwang@buaa.edu.cn

ABSTRACT

The evolution of entrainment in the separated and reattaching flow induced by a wall-mounted fence are studied by means of particle image velocimetry (PIV) experiments in the water tunnel. The flow undergoes the transition process of separation, reattachment and the development of the new turbulent boundary layer until it is fully developed. In this transition process, the entrainment also evolves in accordance with the development of flow. The entrainment velocity is modulated by vortex structures: the entrainment velocity decreases above the prograde vortex while it increases significantly above the retrograde vortex near the turbulent/non-turbulent interface. As a result of the modulation of vortex structures, the entrainment velocity is the smallest along the streamwise direction where the prograde shedding vortex is strong when deforming due to the secondary instability, while the entrainment velocity increases significantly when strong retrograde vortices appears after the breakdown of shedding vortices. The global peak of the mean entrainment velocity appears after the reattachment, which is not related to the effect of vortex structures.

INTRODUCTION

Many studies have demonstrated the existence of a thin and distorted layer that demarcates the turbulent and non-turbulent regions in turbulent shear flows such as jets, mixing layers and boundary layers. This layer is commonly known as the turbulent/non-turbulent interface (TNTI) and has become an important focus in the study of instantaneous entrainment characteristics (Da Silva *et al.*, 2014). Entrainment refers to the processes by which fluid in the non-turbulent region is continually drawn into the turbulent region, leading to the increase of the extent of the turbulent region. Generally, it is agreed that entrainment is achieved in two ways, which are anthropomorphically called engulfment and nibbling, respectively. Engulfment is an inviscid process that occurs locally and occasionally, in which the fluid outside the interface is swallowed by the turbulent region. Nibbling happens continuously along the entire interface which is mainly caused by viscous vorticity propagation. It is indicated that the contribute of nibbling to entrainment accounts for the majority in many flows (Westerweel *et al.*, 2005; Jahanbakhshi & Madnia, 2016; Long *et al.*, 2022a). Therefore, more attention has been attached to the characteristics of nibbling rather than engulfment.

To gain deeper insights into the mechanisms of entrainment, the effect of turbulent coherent structures on entrainment has attracted considerable attention. It was reported that local entrainment is mostly controlled by small-scale motions (Westerweel *et al.*, 2009). The local entrainment velocity, which is commonly used to quantify the nibbling process, is modulated by the nearby Taylor-microscale eddies (Mistry *et al.*, 2019; Neamtu-Halic *et al.*, 2020). Meanwhile, some other works indicated that the large-scale motions also play an important role in local entrainment (Philip *et al.*, 2014; Long *et al.*, 2022a). Long *et al.* (2022a) reported that low-speed large-scale motions could induce stronger instantaneous nibbling, but the integral nibbling flux is larger above high-speed motions due to the more distorted TNTI induced by high-speed large-scale motions.

When most detailed researches focus on entrainment in fully developed turbulent flows, some have shown the characteristics of entrainment in spacially developing flows. Zhang *et al.* (2021) studied the TNTI properties in the airfoil flow. They reported that the dependency of local entrainment on the TNTI geometry after the transition is analogous to that in the jets and wakes, but in the early transitional stage the entrainment is not modified by the geometric properties of the TNTI. Long *et al.* (2022b) explored the evolution of entrainment in the transitional boundary layer over a multi-element airfoil, and indicated that the increase of the TNTI length has a greater effect on entrainment than the decrease of the vorticity gradient during transition, resulting in the increases of local entrainment flux along the streamwise direction.

Despite of the investigation on the development of entrainment, the effect of flow structures on entrainment in the transition process needs to be further studied. Thus, the goal of the present work is to study the evolution of the turbulent entrainment in spacially developing flows e.g. separated and reattaching turbulent flows, and assess the effect of flow structures on the entrainment. For this purpose, experiments were
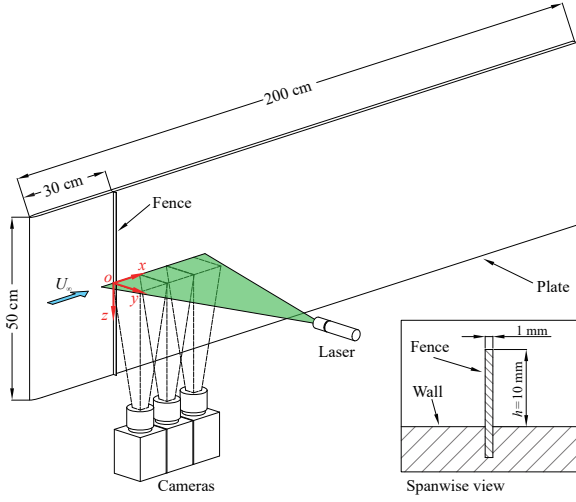
Figure 1: Schematic of the experimental setup.

Figure 2: Visualization of the instantaneous vorticity field downstream of the fence. The TNTI is denoted by the black solid line.

carried out where the separated and reattaching flows is induced by a wall-mounted fence in the flat-plate boundary layer.

EXPERIMENTAL SETUP

The time-resolved particle image velocimetry (PIV) experiments were conducted in the low-speed water channel at Beihang University. The experimental setup is illustrated in figure 1. A flat and smooth acrylic plate was vertically fixed in the center of the 3-meter-long, 60-centimeter-wide channel. The length, width and thickness of the plate were 200, 50 and 1.5 cm, respectively, and the free surface of water just submerged the top of the plate. An elliptic leading edge with the aspect ratio of 5 : 1 was utilized to avoid flow separation from the leading edge of the plate, maintaining the flow laminar before the disturbance of fence. The flow separation was induced by a stainless steel fence mounted on the plate as shown in the lower-right subgraph of figure 1. The fence was 10 mm in height (denoted as h), 1 mm in thickness and 30 cm away from the leading edge of the plate. The freestream velocity U_∞ is 102 mm/s and the Reynolds number based on the height h is $Re_h = U_\infty h / \nu = 965$, where ν is the kinematic viscosity.

The two-dimensional PIV system was used to capture the velocity field. The fields of view (FoV) were located in the central plane of the plate, which were far away from both the free surface and the bottom wall of the channel to minimize the end effect. Seeding particles were hollow glass beads with a diameter of 5–20 μm and a density of 1.05 g/cm^3, which were lightened by a laser sheet approximately 1 mm thick produced by a high-frequency double-pulsed laser (Beamtech Vlite-Hi-527-30k). The particle images were synchronously captured by three CMOS cameras (2048 × 2048 pixels) with Nikkor 85-mm tilt-shift lenses, with a sampling frequency of 250 Hz. The FoV for each camera was approximately $10h \times 10h$ and there was an overlap of at least 10 mm between the FoVs of adjacent cameras. Calibration with a single long reference target covering the entire measurement area was used for stitching FoVs. To obtain a longer velocity field on this basis to analyze the evolution of entrainment, measurements were repeated three times at different stations with each measurement covering a streamwise region of approximately $25h$, limited by the width of the laser sheet. The multiple iterative Lucas–Kanade algorithm (Pan *et al.*, 2015) is used to calculate the velocity field with an interrogation window of 32 × 32 pixels and an over-
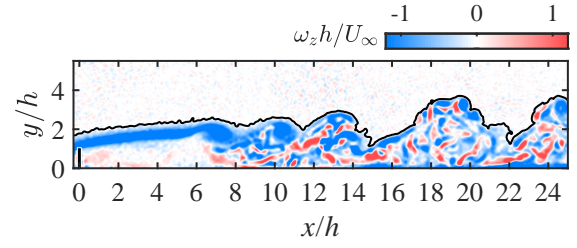
lap of 75% for the final iteration. The velocity vector spacing scales at the Kolmogorov scale η_I measured on the TNTI, indicating that the present spatial resolution is high enough and suffices for the TNTI detection and relevant analyses. The velocity uncertainty ε_u was approximately 1.21 mm/s, and the relative velocity uncertainty ε_u/U_∞ was approximately 1.2%. The vorticity uncertainty ε_{ω_z} was obtained following Qu *et al.* (2019), which was approximately 2.32 s^{-1}, and the normalized vorticity uncertainty $\varepsilon_{\omega_z} h / U_\infty$ equals 0.23.

RESULTS AND DISCUSSION
Development of the flow field

Generally, the vorticity of the turbulent flow is much higher than that of non-turbulent flows, so the vorticity magnitude (or the enstrophy) is usually used to detect this irrotational boundary between turbulent and non-turbulent regions. In the present work, spanwise enstrophy $\omega_z^2 = (\partial v / \partial x - \partial u / \partial y)^2$ is used to detect the interface, and the procedure is the same as our previous work (Li *et al.*, 2022). An instantaneous vorticity field superimposed with the TNTI is shown in figure 2. Meanwhile, a clear development process of the separated shear layer can be observed, which is similar to the development of the bluff body shear layer (Lander *et al.*, 2016), that is, the separated shear layer rolls up forming the shedding vortex, and then the shedding vortex deforms and breaks down into small-scale eddies. It should be noted that in the initial stage, the separated shear appears laminar, which makes it debatable to call this irrotational interface "TNTI". Nevertheless, the detection procedure is consistent with the detection of TNTI in fully developed turbulence (Da Silva *et al.*, 2014; Long *et al.*, 2022a). In addition, when the downstream boundary layer is fully developed, the present results could be consistent with the existing turbulent entrainment conclusions. As a consequence, following previous practices (Philip *et al.*, 2015; Long *et al.*, 2022b), the interface herein is also referred to as TNTI for convenience.

To statistically quantify the development process of the shear layer, the vorticity thickness is investigated, which is defined as $\delta_v = (U_{\max} - U_{\min})/(\partial U / \partial y)_{\max}$, where $U_{\max}$ and $U_{\min}$ are the maximum and minimum mean streamwise velocity, respectively, and $(\partial U / \partial y)_{\max}$ is the maximum vertical gradient of the mean streamwise velocity. The vorticity thickness δ_v increases along streamwise direction with four different slopes as shown in figure 3(*a*). The change of vorticity thickness slope indicates the development of flow structure (Fang & Tachie, 2019; Kang *et al.*, 2021). Drawing on the past understanding of the evolution of separate shear layers (Lander *et al.*, 2016) and the observation of instantaneous motions, the development of the separated shear layer in the present case is divided into four stages based on the charac-
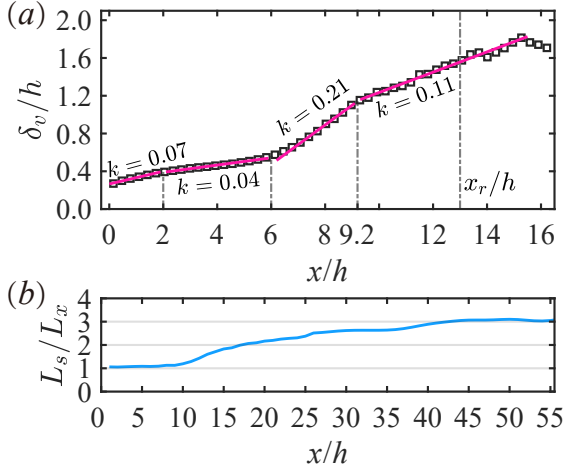
Figure 3: (a) Streamwise variation of vorticity thickness δ_v. The magenta solid lines represent the linear fits to vorticity thickness. $k = d\delta_v/dx$ is the growth rate of vorticity thickness. x_r is the location of the reattachment point. (b) Tortuosities of the TNTI at different streamwise positions.
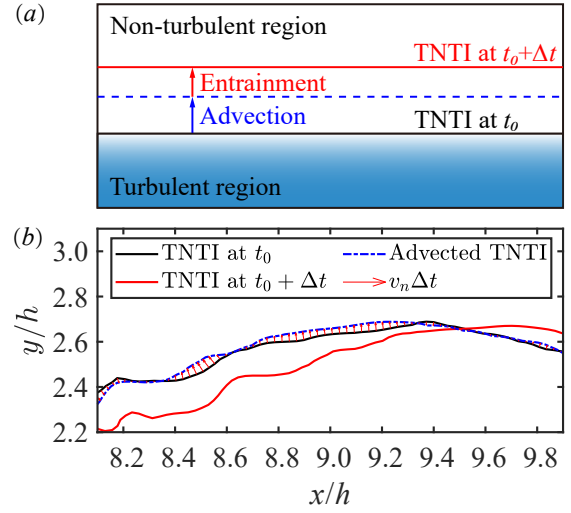

Figure 4: (a) Illustration of the interface movement as a result of advection and entrainment. (b) Illustration of the interface-tracking method for obtaining the entrainment velocity.

teristic points of the vorticity thickness, i.e. the laminar shear stage when $x < 2h$, vortex generation and growth stage when $x \in [2h, 6h]$, vortex deformation stage when $x \in [6h, 9.2h]$ and vortex breakdown stage after $x > 9.2h$.

In the early stages when $x < 6h$, the irrotational interface is relatively flat and stable. When the shedding vortex deforms significantly, the position of the interface begins to fluctuate up and down. Further, after the breakdown of the shedding vortex when $x > 9.2h$, the shape of the TNTI becomes more distorted. To quantitatively reflect the evolution of the TNTI geometry, the tortuosity is investigated, which is defined as the length of TNTI curve per streamwise distance L_s/L_x. As shown in figure 3(b), $L_s/L_x \approx 1$ before the shedding vortex breaks down into turbulent eddies, while the tortuosity of TNTI begins to increases monotonously after $x > 9.2h$. Finally, it reaches a new plateau of $L_s/L_x \approx 3$ when the new turbulent boundary layer is fully developed after $x > 46h$.

Development of the entrainment velocity

The entrainment velocity v_n is the velocity of the TNTI relative to the flow, which has been extensively studied to quantitatively understand local entrainment (Holzner & Luthi, 2011; Mistry *et al.*, 2016; Long *et al.*, 2022a). It is generally believed that the movement of TNTI is composed of the advection with local flow and the displacement caused by local entrainment, as illuminated in figure 4(a). As a consequence, to obtain the entrainment velocity v_n, the interface-tracking method proposed by Wolf *et al.* (2012) is implemented. Figure 4(b) shows an example of this procedure for obtaining v_n via the interface-tracking method. First, the TNTI at a short time interval after $(t_0 + \Delta t)$ is advected with the local velocity back to the current instant t_0, which is called the advected TNTI. Second, calculating the distance along the normal direction from the TNTI at t_0 to the advected TNTI. Third, the entrainment velocity is obtained by dividing the normal distance with the advection time Δt. In practice, the selection of Δt lacks a uniform standard, which depends on the data set and flow type being considered. Mistry *et al.* (2016) studied the effect of Δt on the statistics of v_n, based on which they car-

ried out the optimum Δt for their case. Following this idea, the variation of mean entrainment velocity $\overline{v_n}$ against Δt was examined and $\Delta t = 0.5\tau_\eta$ was selected because results were least sensitive to Δ around here, where τ_η is the local Kolmogorov time scale.

The streamwise variation of the mean entrainment velocity $\overline{v_n}$ is shown in figure 5. Note that, since the interface normal vector is defined to point towards the turbulent region, a negative v_n corresponds to entrainment causing the extension of the turbulent region. When $x < 2h$, the separated flow is dominant by the shear motions and the increase of $\overline{v_n}$ is quite small. When the shedding vortex appears $(x > 2h)$, the entrainment velocity begins to decrease. The magnitude of $\overline{v_n}$ decreases more quickly when the vortex structure begins to deform due to secondary instability when $x > 6h$. The entrainment velocity is minimum at $x = 7.5h$ where the shedding vortex is the strongest. With the further deformation of the shedding vortex, the vortex structure is stretched more significantly in the vertical direction and the entrainment velocity begins to recovery gradually. After the breakdown of the shedding vortex, the mean entrainment velocity continues to increase and and reaches the maximum magnitude of $|\overline{v_n}| = 1.85u_\eta$ downstream of the reattachment point, where u_η is the local Kolmogorov velocity scale. The mean entrainment velocity decreases monotonously downstream of its global peak. Finally, when the turbulent boundary layer is fully developed $(x > 46h)$, $|\overline{v_n}|$ decreases back to a constant value of $0.85u_\eta$, which is consistent with results reported by previous studies for fully developed turbulence (Wolf *et al.*, 2012; Mistry *et al.*, 2016; Long *et al.*, 2022b).

Modulation of vortex structures on the entrainment velocity

Since the vortex near the TNTI could modify the local entrainment velocity Neamtu-Halic *et al.* (2020), it is not difficult to consider that the variation of the entrainment velocity is related to the development of the shedding vortex. In the present work, vortex structures are detected by swirling strength criterion (Zhou *et al.*, 1999). In this criterion, the swirling strength of vortex structure is represented by the mag-
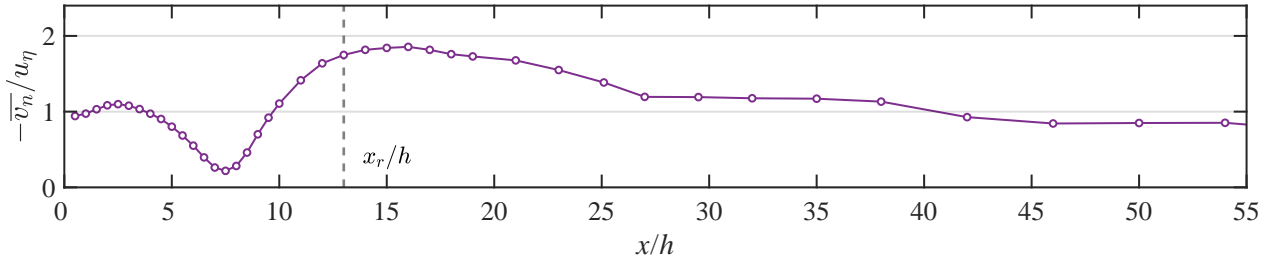
3

Figure 5: Streamwise variation of the mean entrainment velocity $\overline{v_n}$. The location of the reattachment point is marked with the vertical dashed line.

nitude of the imaginary part of the eigenvalue of the velocity gradient tensor $|\lambda_{ci}|$, and the sign of λ_{ci} is set to be the same as that of the local spanwise vorticity to distinguish spanwise vortices with different swirling directions. Herein, the prograde vortex refers to the spanwise vortex that rotates in the same sence as the mean shear ($\lambda_{ci} < 0$), while the retrograde vortex is the opposite ($\lambda_{ci} > 0$).

To more profoundly study the effect of vortex structures on entrainment, the entrainment velocities are conditionally averaged based on whether there is prograde, retrograde or no vortex structure beneath the TNTI, which are denoted by $\langle v_n \rangle_p$, $\langle v_n \rangle_r$ and $\langle v_n \rangle_0$, respectively. When there is no vortex structure beneath the TNTI, the conditional averaged entrainment velocity $\langle v_n \rangle_0$ is almost constant when $x < 9.2h$ as shown in figure 6(a). Subsequently, $\langle v_n \rangle_0$ increases after the breakdown of the prograde shedding vortex and declines downstream of its global peak which is at the same streamwise location as that of the time mean entrainment velocity. Thereafter, the effect of vortex structure on entrainment is recognizable by comparing with the no-vortex case.

Around the retrograde vortex structures, the entrainment velocity is dramatically enhanced, with the maximum 2.4 times as large as that of $\langle v_n \rangle_0$ at $x = 11h$. After $x > 11$, $\langle v_n \rangle_r$ decreases monotonously, and it becomes constant when the boundary layer is fully developed ($x > 46h$). On the other hand, the prograde vortex shows obvious suppression effect on the entrainment process, causing $\langle v_n \rangle_p$ to be smaller than $\langle v_n \rangle_0$ when $x > 4h$. The decrease of v_n does not occur from the generation of the prograde shedding vortex in $x \in [2h, 4h]$, indicating that the weak vortex generated in the early stage are difficult to affect entrainment. The greatest reduction of the entrainment velocity appears at $x = 7.5h$. It is noticeable that when the modulation of the prograde vortex is strongest in the vicinity of $x = 7.5h$, $\langle v_n \rangle_p$ even becomes positive corresponding to the detrainment process. After the breakdown of the shedding vortex, $\langle v_n \rangle_p$ shows the similar variation trend with $\langle v_n \rangle_0$ as the effect of the prograde vortex weakens. When the boundary layer is fully developed, the conditional averaged entrainment velocities become constant, while the entrainment velocity above the retrograde vortex is still slightly larger than the other conditional averaged entrainment velocities. In the transition process, the streamwise locations of the greatly enhanced and reduced local entrainment velocities are consistent well with the extreme circulations of retrograde vortices and prograde vortices, respectively, as shown in figure 6(b). The circulation Γ is obtained by integrating the vorticity in the domain of the vortex structure, and $\overline{\Gamma}$ refers to the time mean circulation. This shows that the local entrainment velocity is related to the strength of the vortex structures in the vicinity of the TNTI in the transition process.

The comparison between cases shows that the decrease in the time mean entrainment velocity is caused by the growth of the progressive shedding vortex before the breakdown. However, the global peak of the mean entrainment velocity is not caused by the modulation of the retrograde vortex. According to Holzner & Luthi (2011), the entrainment velocity is related to vorticity strain motion, viscous diffusion and dissiaption. We suspect that the global peak of entrainment velocity in the separated and reattaching flow is more related to the variation of vorticity viscous propagation rather than to the effect of vortex structures. Due to the lack of three-dimensional data, it is difficult to obtained direct evidences, and more studies will be conducted in the future to gain a deeper understanding.

CONCLUSION

The evolution of entrainment in the separated and reattaching flow induced by a wall-mounted fence are studied by the time-resolved particle image velocimetry experiments in the water tunnel. The flow undergoes the transition process of separation, reattachment and the development of the new turbulent boundary layer until it is fully developed. Significant variations of entrainment occur mainly above the recirculation zone and the reattachment zone. The local entrainment velocity decreases above the prograde vortex, while it increases significantly above retrograde vortices near the TNTI. As a result of the modulation of vortex structures, the mean entrainment velocity is the smallest along the streamwise direction where the prograde shedding vortex is strong when deforming due to the secondary instability. The conditional averaged entrainment velocity above retrograde vortices increases significantly when strong retrograde vortices appears after the breakdown of shedding vortices. However, the global peak of the mean entrainment velocity appears after the reattachment, which is not related to the effect of vortex structures.

REFERENCES

Da Silva, C., Hunt, J. C. R., Eames, I. & Westerweel, J. 2014 Interfacial layers between regions of different turbulence intensity. *Annu. Rev. Fluid Mech.* **46(1)**, 567–590.

Fang, X. & Tachie, M. F. 2019 On the unsteady characteristics of turbulent separations over a forward-backward-facing step. *J. Fluid Mech.* **863**, 994–1030.

Holzner, M. & Luthi, B. 2011 Laminar superlayer at the turbulence boundary. *Phys. Rev. Lett.* **106(13)**, 134503.

Jahanbakhshi, R. & Madnia, C. 2016 Entrainment in a compressible turbulent shear layer. *J. Fluid Mech.* **797**, 564–603.

Kang, N., Essel, E. E., Roussinova, V. & Balachandar, R. 2021 Effects of approach flow conditions on the unsteady three-
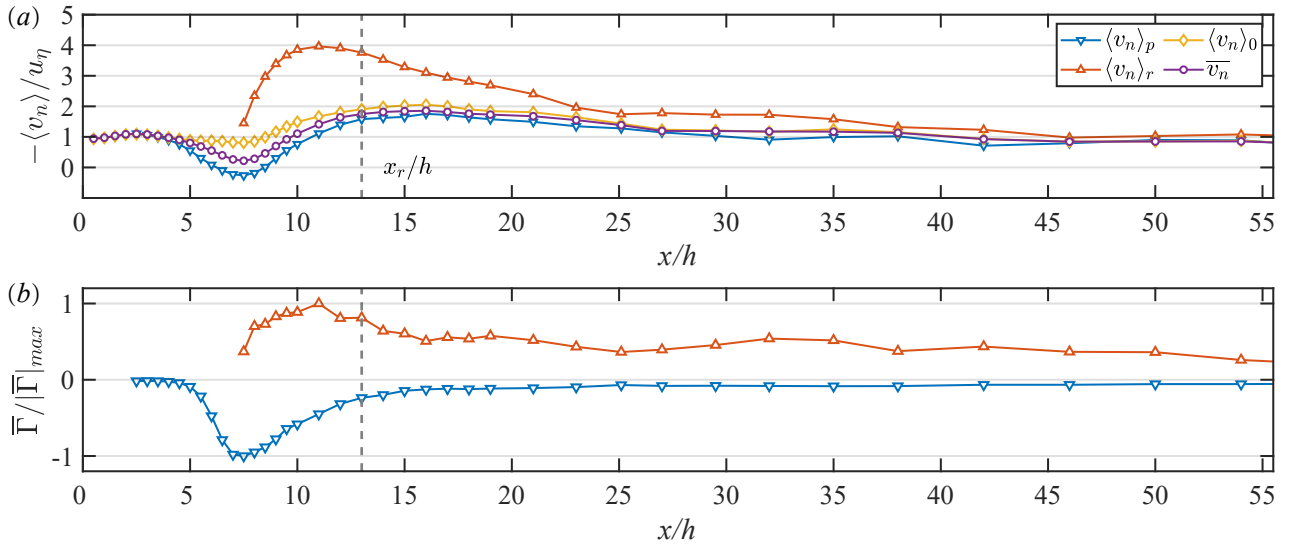
Figure 6: (*a*) Streamwise variations of the conditional averaged entrainment velocity $\langle v_n \rangle$ based on whether there is prograde, retrograde or no vortex structure beneath the TNTI, respectively. The time mean entrainment velocity $\overline{v_n}$ is also plotted for comparison. (*b*) Streamwise variation of the mean circulations $\overline{\Gamma}$ of prograde and retrograde vortex structures, which are normalized by their global maximum, respectively. The location of the reattachment point is marked with the vertical dashed line.

dimensional wake structure of a square-back ahmed body. *Phys. Rev. Fluids* **6(3)**, 034613.

Lander, D. C., Letchford, C. W., Amitay, M. & Kopp, G. A. 2016 Influence of the bluff body shear layers on the wake of a square prism in a turbulent flow. *Phys. Rev. Fluids* **1**, 044406.

Li, S., Long, Y. & Wang, J. 2022 Turbulent/non-turbulent interface for laminar boundary flow over a wall-mounted fence. *Phys. Fluids* **34**, 125113.

Long, Y., Wang, J. & Pan, C. 2022*a* Universal modulations of large-scale motions on entrainment of turbulent boundary layers. *J. Fluid Mech.* **941**, A68.

Long, Y., Wang, J. & Wang, J. 2022*b* "turbulent/non-turbulent interface" in a low-reynolds-number transitional boundary layer over a multi-element airfoil. *Phys. Fluids* **34**, 102111.

Mistry, D., Philip, J. & Dawson, J. 2019 Kinematics of local entrainment and detrainment in a turbulent jet. *J. Fluid Mech.* **871**, 896–924.

Mistry, D., Philip, J., Dawson, J. R. & Marusic, I. 2016 Entrainment at multi-scales across the turbulent/non-turbulent interface in an axisymmetric jet. *J. Fluid Mech.* **802**, 690–725.

Neamtu-Halic, M. M., Krug, D., Mollicone, J., van Reeuwijk, M., Haller, G. & Holzner, M. 2020 Connecting the time evolution of the turbulence interface to coherent structures. *J. Fluid Mech.* **898**, A3.

Pan, C., Xue, D., Xu, Y., Wang, J. & Wei, R. 2015 Evaluating the accuracy performance of lucas-kanade algorithm in the circumstance of piv application. *Sci. China-Phys. Mech. Astron.* **58**, 104704.

Philip, J., Bermejo-Moreno, I., Chung, D. & MARUSIC, I. 2015 Characteristics of the entrainment velocity in a developing wake. In *International Symposium on Turbulence and Shear Flow Phenomena*, *TSFP-9*, vol. 3. Melbourne, Australia.

Philip, J., Meneveau, C., de Silva, C. M. & Marusic, I. 2014 Multiscale analysis of fluxes at the turbulent/non-turbulent interface in high reynolds number boundary layers. *Phys. Fluids* **26(1)**, 015105.

Qu, Y., Wang, J., Feng, L. & He, X. 2019 Effect of excitation frequency on flow characteristics around a square cylinder with a synthetic jet positioned at front surface. *Journal of Fluid Mechanics* **880**, 764–798.

Westerweel, J., Fukushima, C., Pedersen, J. M. & Hunt, J. C. R. 2005 Mechanics of the turbulent-nonturbulent interface of a jet. *Phys. Rev. Lett.* **95(17)**, 174501.

Westerweel, J., Fukushima, C., Pedersen, J. M. & Hunt, J. C. R. 2009 Momentum and scalar transport at the turbulent/non-turbulent interface of a jet. *J. Fluid Mech.* **631**, 199–230.

Wolf, M., Lüthi, B., Holzner, M., Krug, D., Kinzelbach, W. & Tsinober, A. 2012 Investigations on the local entrainment velocity in a turbulent jet. *Phys. Fluids* **24** (10), 105110.

Zhang, H., Rival, D. E. & Wu, X. 2021 Kinematics of the turbulent and nonturbulent interfaces in a subsonic airfoil flow. *AIAA Journal* **59** (6), 2155–2168.

Zhou, J., Adrian, R. J., Balachandar, S. & Kendall, T. M. 1999 Mechanisms for generating coherent packets of hairpin vortices in channel flow. *J. Fluid Mech.* **387**, 353–396.